Using the moments of a thick layer to map conductance and conductivity from airborne electromagnetic data

Richard S. Smith [a,*], Terry J. Lee [b]

[a]*Fugro Airborne Surveys, 2060 Walkley Road, Ottawa, Ontario, Canada K1G 3P5*
[b]*P.O. Box 1984, Canberra, A.C.T., 2601, Australia*

Abstract

The moments of the airborne electromagnetic impulse response have been derived for a thick horizontal layer. These moments can be written in an analytic form for the first- and second-order moments, both for the horizontal component and the vertical component. In the limiting case of a thin sheet, the horizontal component has first-, second- and third-order moments, while the vertical component has first- and second-order moments. On the other hand, the limiting case of a half space only has first-order moments for both components. The analytic expressions for the moments can be inverted analytically, so that the half space conductivity, thin-sheet conductance, and conductivity and thickness can be estimated. The images derived from the higher-order moments better identify a deeper conductor. This is consistent with the higher-order moments being more responsive to deeper material. © 2002 Elsevier Science B.V. All rights reserved.

Keywords: Airborne; Electromagnetics; Moments; Conductance; Conductivity

1. Introduction

Traditional methods of interpreting time-domain electromagnetic data generally work with the decay information, analyzing or fitting the transient response. Recently, Smith and Lee (in press) have introduced a new paradigm for the interpretation of the time-domain data: the concept of the moments of the impulse response. If the impulse response as a function of time t is denoted as $I(t)$, then the nth moment M^n is given by

$$M^n = \int_0^\infty I(t)t^n \mathrm{d}t. \tag{1}$$

These moments have been shown (Smith and Lee, in press) to be a generalization of the concepts of the inductive limit (zeroth moment) and the resistive limit (first moment) used in the interpretation of frequency-domain data (Grant and West, 1965) and time-domain data (Macnae et al., 1998, 1999).

For the case of a sphere excited by a dipolar magnetic field, the moments can be written as a sum over the zeros of the Bessel functions (Smith and Lee, in press). For the case of a sphere in a uniform field,

* Corresponding author. Tel. +1-613-731-9575; fax: +1-613-731-0453.
E-mail addresses: rsmith@fugroairborne.com (R.S. Smith), TerryLJee@bigpond.com (T.J. Lee).

the sum of the zeros simply include the Bernoullian numbers (Smith and Lee, 2001). If the model is a wire loop circuit (Grant and West, 1965), the nth moment is $n!\tau^n$, where τ is the time constant of the circuit (Smith and Lee, in press). In each case, the analytic forms of the moments are much simpler than the full transient response and even the frequency-domain response. Hence, it is computationally easier to model the moments than the full transient response and should also be easier to invert the moments to estimate the physical properties of the ground.

In this paper, we derive the moments of a thick layer of infinite horizontal extent: the first- and second-order moments have simple analytic forms. The limiting cases of a thin sheet and a conductive half space also have analytic expressions for some of the low order moments. These analytic expressions can be inverted analytically and used to generate conductance, conductivity and thickness maps.

2. The moments of a thick layer

The secondary magnetic field above an earth excited by a vertical magnetic dipole is given by Ward and Hohmann (1988) as

$$H_\rho(\rho, z) = \frac{m_{TX}}{4\pi} \int_0^\infty r_{TE} e^{\lambda(z-h)} \lambda^2 J_1(\lambda\rho) d\lambda, \tag{2}$$

$$H_z(\rho, z) = \frac{m_{TX}}{4\pi} \int_0^\infty r_{TE} e^{\lambda(z-h)} \lambda^2 J_0(\lambda\rho) d\lambda, \tag{3}$$

where H_i is the magnetic field in the ith direction, z and ρ are the vertical and horizontal position of the receiver, h is the transmitter height, r_{TE} is the reflection coefficient of the TE mode, λ is the Hankel transform variable, m_{TX} is the transmitter dipole moment and J_l is the Bessel function order l. The sign convention used has z negative and h positive for receivers above the ground. The term associated with the primary field in Eqs. (4.45) and (4.46) of Ward and Hohmann has been dropped and we have set $u_0 = \lambda$.

If we assume the quasistatic limit and that the permeability is everywhere equal to the free space value, then for a thick layer, with conductivity σ and thickness d, and insulators above and below, the reflection coefficient, given in Ward and Hohmann, reduces to

$$r_{TE} = \frac{-i\omega\mu\sigma\tanh(ud)}{2\lambda u + \tanh(ud)(\lambda^2 + u^2)}, \tag{4}$$

where $u = \sqrt{\lambda^2 + i\omega\mu\sigma}$. The denominator is of the form

$$D(u) = 2\lambda u + \tanh(ud)(\lambda^2 + u^2). \tag{5}$$

If we put $u = im$, then

$$D(m) = i[2\lambda m + \tan(md)(\lambda^2 - m^2)], \tag{6}$$

where we have used the relation between circular and hyperbolic tangents [Abramowitz and Stegun, 1965, Eq. (4.5.9)]. The only zeros of $D(m)$ are purely real (Carslaw and Jaeger, 1959) and there are no branch cuts. Hence, at the poles, m^2 is both real and positive. Because we have $m^2 = -(\lambda^2 + i\omega\mu\sigma)$, then $\lambda^2 + i\omega\mu\sigma$ must be real and negative. If we denote this negative number $-a$, where a is real and positive, then

$$\omega = \frac{i}{\mu\sigma}(\lambda^2 + a). \tag{7}$$

Thus, poles occur where ω is purely imaginary and positive, i.e. on the upper half of the complex plane. The inverse Laplace transform of the reflection coefficient is given by

$$R_{TE}(t) = \frac{1}{2\pi i} \int_C e^{st} r_{TE}(s) dt, \tag{8}$$

where C is the Bromwich contour. We can make the substitution, $s = i\omega = -z$ and use the residue theorem to evaluate the integral

$$R_{TE}(t) = \sum_k e^{-z_k t} \lim_{z \to z_k} (z - z_k) r_{TE}(z) \tag{9}$$

where z_k are the positive real roots of r_{TE}. The moments of the reflection coefficient are

$$I_r^n = \int_0^\infty R_{TE} t^n dt, \tag{10}$$

or,

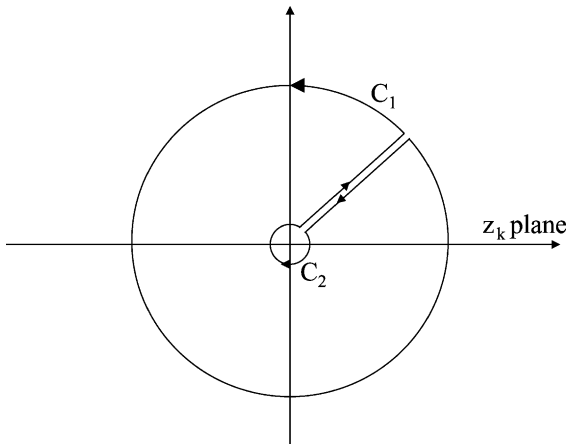$$I_r^n = \sum_k \frac{n!}{z_k^{n+1}} \lim_{z \to z_k} (z - z_k) r_{TE}(z), \tag{11}$$

Fig. 1. The contour path used for integration of Eq. (13).

where we have used the relation

$$\int_0^\infty t^n e^{-z_k t} dt = \frac{n!}{z_k^{n+1}}.$$ (12)

In order to evaluate Eq. (11), we recognize that the residue theorem can be used to write this expression in the form of a contour integral

$$I_r^n = \frac{1}{2\pi i} \int_C \frac{n!}{z^{n+1}}$$

$$\times \frac{z\mu\sigma\tanh(ud)}{2\lambda u + \tanh(ud)(\lambda^2 + u^2)} dz,$$ (13)

where C is a closed contour. This can be evaluated by deforming the contour C into two components C_1 and C_2, as shown in Fig. 1. The radial paths are chosen to be sufficiently close to each other and sufficiently far from the zeros of D, that the inward and outward segments cancel. The outer circle C_1 is at very large radial distances R, and C_2 encloses the zeros of z^{n+1}.

The $n=0$ case must be considered separately. In this instance, we first consider the integral around the outer circle C_1. Here, z is large compared with λ, so $u \rightarrow \sqrt{z\mu\sigma}$ and

$$f(z) = \frac{z\mu\sigma\tanh(ud)}{2\lambda u + \tanh(ud)(\lambda^2 + u^2)} \rightarrow 1.$$ (14)

Hence, the integral becomes

$$\frac{1}{2\pi i} \int_{C_1} \frac{1}{z} dz = 1,$$ (15)

from Cauchy's formula. On the inner contour C_2, we have

$$\frac{1}{2\pi i} \int_{C_2} \frac{f(z)}{z} dz = 0,$$ (16)

as $f(z) \rightarrow 0$ as $z \rightarrow 0$. Hence, $I_r^0 = 1$.

For the cases when $n > 0$, we use the same contour path as shown in Fig. 1. For large R, $f(z) \rightarrow 1$, but $n!/z^{n+1} \rightarrow 0$, so the integral around C_1 has no contribution. Hence,

$$I_r^n = \frac{n!}{2\pi i} \int_{C_2} \frac{f(z)}{z^{n+1}} dz.$$ (17)

Using Cauchy's integral formula, Eq. (17) becomes

$$I_r^n = f^n(0),$$ (18)

where $f^n(z)$ denotes the nth derivative with respect to the argument evaluated at z. Differentiation of $f(z)$ and substitution of $z=0$ yields after some simplifications

$$I_r^1 = \frac{\mu\sigma}{4\lambda^2} \left[1 - e^{-2\lambda d} \right].$$ (19)

$$I_r^2 = -2 \left(\frac{\mu\sigma}{2\lambda^2} \right)^2 \left[e^{-\lambda d}\sinh(\lambda d) - e^{-2\lambda d}\lambda d \right].$$ (20)

We return now to evaluating the moments of the magnetic-field impulse response as defined by Eq. (1). The moment integral for the reflection coefficient has already been evaluated, so all that remains is the λ integration in Eqs. (2) and (3). The nth moments for the ρ and z components are

$$M_\rho^n = \frac{m_{TX}}{4\pi} \int_0^\infty I_r^n e^{\lambda(z-h)}\lambda^2 J_1(\lambda\rho)d\lambda,$$ (21)

$$M_z^n = \frac{m_{TX}}{4\pi} \int_0^\infty I_r^n e^{\lambda(z-h)}\lambda^2 J_0(\lambda\rho)d\lambda.$$ (22)

For the zeroth-order moment, we use $I_r^0 = 1$, giving

$$M_j^0 = \frac{m_{TX}}{4\pi} \int_0^\infty e^{\lambda(z-h)}J_l(\lambda\rho)d\lambda,$$ (23)

where $l=1$ when $j=\rho$ and $l=0$ when $j=z$. For the ρ component, this can be written

$$M_\rho^0 = \frac{-m_{TX}}{4\pi} \frac{\partial^2}{\partial\rho\partial z} \int_0^\infty e^{\lambda(z-h)}J_0(\lambda\rho)d\lambda,$$ (24)

which on substitution of Eq. (A1) and subsequent differentiation becomes

$$M_\rho^0 = \frac{-m_{TX}}{4\pi} \frac{3\rho(z-h)}{(\rho^2 + (z-h)^2)^{5/2}}. \tag{25}$$

Similarly, for the z component

$$M_z^0 = \frac{m_{TX}}{4\pi} \frac{\partial^2}{\partial z^2} \int_0^\infty e^{\lambda(z-h)} J_0(\lambda\rho) d\lambda, \tag{26}$$

which can be similarly simplified to give

$$M_z^0 = \frac{m_{TX}}{4\pi} \frac{2(z-h)^2 - \rho^2}{(\rho^2 + (z-h)^2)^{5/2}}. \tag{27}$$

The expressions (25) and (27) are equivalent to the magnetic field of an image at a depth h below the ground surface. The zeroth-order moment is only dependent on the geometric configuration of the EM system—there is no dependence on the conductivity or conductance—so these expressions are of no value in mapping these quantities. This image response is equivalent to the inductive limit, or early-time response for a thin sheet or half space (Grant and West, 1965).

For the first-order moment, substitution of Eq. (19) gives

$$M_j^1 = \frac{m_{TX}}{4\pi} \frac{\mu\sigma}{4} \int_0^\infty e^{\lambda(z-h)} J_l(\lambda\rho) \\ - e^{-\lambda(2d+h-z)} J_l(\lambda\rho) d\lambda, \tag{28}$$

where once again $l = 1$ when $j = \rho$ and $l = 0$ when $j = z$. For the M_ρ^1 case, we can use Eq. (A2) from Appendix A to write

$$M_\rho^1 = \frac{m_{TX}}{4\pi} \frac{\mu\sigma}{4} \left[\frac{1}{\rho} \left(1 - \frac{h-z}{\sqrt{\rho^2 + (h-z)^2}} \right) \\ - \frac{1}{\rho} \left(1 - \frac{2d+h-z}{\sqrt{\rho^2 + (2d+h-z)^2}} \right) \right], \tag{29}$$

which simplifies to

$$M_\rho^1 = \frac{m_{TX}}{4\pi} \frac{\mu\sigma}{4} \frac{1}{\rho} \left[\left(\frac{h-z}{\sqrt{\rho^2 + (h-z)^2}} \right) \\ - \left(\frac{2d+h-z}{\sqrt{\rho^2 + (2d+h-z)^2}} \right) \right], \tag{30}$$

for the horizontal component. Note that in the limit as $d \to \infty$, this expression cannot be used; it is necessary to re-derive the expression after dropping the second term in Eq. (28). The re-derived expression is the first term in the square brackets of Eq. (29).

The first-order moment for the vertical component can be evaluated using Eq. (A1)

$$M_z^1 = \frac{m_{TX}}{4\pi} \frac{\mu\sigma}{4} \left[\left(\frac{1}{\sqrt{\rho^2 + (h-z)^2}} \right) \\ - \left(\frac{1}{\sqrt{\rho^2 + (2d+h-z)^2}} \right) \right]. \tag{31}$$

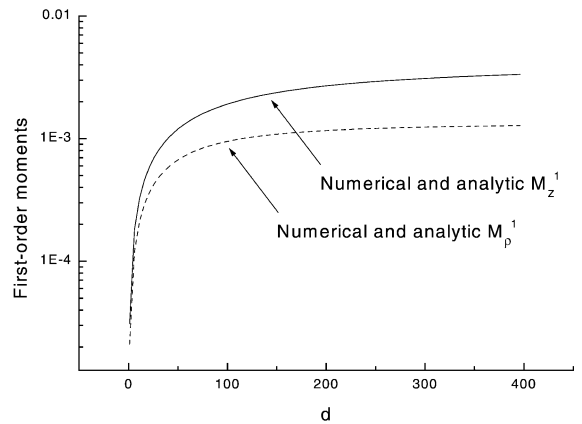In this case, for large d, the second term vanishes, and we are left with the moment for a half space.

Fig. 2. The first-order moments as a function of increasing thickness d, for $\rho = 130$, $h = 120$, $z = -70$, setting $\frac{m}{4\pi} \frac{(\mu\sigma)^2}{2} = 1$. The analytic expressions (Eqs. (30) and (31)) plot on top of the results derived by numerical integration of Eq. (28).

The first-order moments have been calculated for $h = 120$ m, $z = 70$ m and $\rho = 130$ m using the analytic solutions given in Eqs. (30) and (31). These have been compared with a numerical evaluation of Eqs. (21) and (22) using digital linear filters (Anderson, 1979; Johansen and Sorensen, 1979; Christensen, 1990; Mohsen and Hashish, 1994). The numerical and analytic solutions are plotted in Fig. 2 with $\frac{m_{TX}}{4\pi} \frac{\mu\sigma}{4} = 1$, and clearly, the two types of solutions are essentially identical, lying on top of each other.

The second-order moments of the magnetic field are given by

$$M_j^2 = \frac{m_{TX}}{4\pi} \frac{(\mu\sigma)^2}{2} \int_0^\infty \frac{1}{\lambda^2} e^{\lambda(z-h)} \ (\lambda d e^{-2\lambda d}$$
$$- \sinh(\lambda d)e^{-\lambda d})J_l(\lambda\rho)d\lambda. \qquad (32)$$

If the sinh function is written in terms of exponential functions [Abramowitz and Stegun, 1965, Eq. (4.5.1)], it is possible to rewrite Eq. (32) in the following form

$$M_j^2 = \frac{m_{TX}}{4\pi} \frac{(\mu\sigma)^2}{2} \int_h^\infty \int_0^\infty d e^{-\lambda(2d+h'-z)}$$
$$- \int_0^d e^{-\lambda(2d'+h'-z)}dd' \ J_l(\lambda\rho)d\lambda dh' , \qquad (33)$$

where d' is the variable of integration for the third integral. For the case when $j = z$, and $l = 0$, the λ integration can be evaluated using the Lipschitz integral (Eq. (A1)) giving

$$M_z^2 = \frac{m_{TX}}{4\pi} \frac{(\mu\sigma)^2}{2} \int_h^\infty \frac{d}{\sqrt{\rho^2 + H_d'^2}}$$
$$- \frac{1}{2}\text{asinh}\left(\frac{H_d'}{\rho}\right) + \frac{1}{2}\text{asinh}\left(\frac{H_h'}{\rho}\right)dh' , \qquad (34)$$

where $H_d' = 2d + h' - z$ and $H_h' = h' - z$ and the d' integral has also been evaluated. Subsequent evaluation of the h' integral gives

$$M_z^2 = \frac{m_{TX}}{4\pi} \frac{(\mu\sigma)^2}{2} \Big[[d\,\text{asinh}(t)]_{H_d}^\infty/\rho$$
$$- \frac{\rho}{2}\Big\{ \left[t\,\text{asinh}(t) - \sqrt{1+t^2}\right]_{H_d}^\infty/\rho$$
$$- \left[t\,\text{asinh}(t) - \sqrt{1+t^2}\right]_{H_h}^\infty/\rho \Big\} \Big], \qquad (35)$$

where $H_d = 2d + h - z$ and $H_h = h - z$. In the limit as $h \to \infty$, the complete expression for the moment must go to zero. Hence, the upper or infinite limit has to be equal to the lower limit as $h \to \infty$. In this limit, we define $(h - z)/\rho = 1/\varepsilon$, where ε is small, then the lower limit can be written

$$\frac{\rho}{2\varepsilon} \Big[\text{asinh}\left(\frac{1}{\varepsilon}\right) - \text{asinh}\left(\frac{2d}{\rho} + \frac{1}{\varepsilon}\right)$$
$$- \sqrt{1 + \varepsilon^2} + \sqrt{1 + \varepsilon^2 + \left(\frac{2d\varepsilon}{\rho}\right)^2 + \frac{4d\varepsilon}{\rho}} \Big]. \qquad (36)$$

Expanding the square root terms using a binomial series, writing the asinh function in terms of the logarithmic function [Abramowitz and Stegun, 1965, Eq. (4.6.20)], and ignoring terms higher than ε^2, this becomes

$$\frac{\rho}{2\varepsilon} \Bigg[\log\left(\frac{1 + \sqrt{1 + \varepsilon^2}}{1 + \frac{2d\varepsilon}{\rho} + \sqrt{1 + \varepsilon^2 + \left(\frac{2d\varepsilon}{\rho}\right)^2 + \frac{4d\varepsilon}{\rho}}} \right)$$
$$+ \frac{2d\varepsilon}{\rho} + \cdots \Bigg]. \qquad (37)$$

The square roots in the logarithmic function can be further expanded using the binomial theorem, giving after some manipulation

$$\frac{\rho}{2\varepsilon} \Big[\log\left(1 - \frac{2d\varepsilon}{\rho} + \cdots \right) + \frac{2d\varepsilon}{\rho} \Big]. \qquad (38)$$

Using a series expansion for the log function [Abramowitz and Stegun, 1965, Eq. (4.1.24)], we have

$$\frac{\rho}{2\varepsilon} \Big[-\frac{2d\varepsilon}{\rho} + \frac{2d\varepsilon}{\rho} + \cdots \Big], \qquad (39)$$

which is zero for large ε. As the lower limit tends to be zero as $h \to \infty$, the upper limit must also be zero. Hence, the only contribution to the integral is the lower

limit, giving after some rearrangement, the required result

$$M_z^2 = \frac{m_{TX}}{4\pi} \frac{(\mu\sigma)^2}{2} \left[\frac{H_h}{2} \log\left(\frac{H_h + \sqrt{\rho^2 + H_h^2}}{H_d + \sqrt{\rho^2 + H_d^2}} \right) \right. $$
$$\left. + \frac{1}{2}\left(\sqrt{\rho^2 + H_d^2} - \sqrt{\rho^2 + H_h^2} \right) \right]. \qquad (40)$$

For the case when $j = \rho$ and $l = 1$, Eq. (33) can be written

$$M_\rho^2 = \frac{m_{TX}}{4\pi} \frac{(\mu\sigma)^2}{2} \int_0^\infty \frac{J_1(\lambda\rho)}{\lambda}$$
$$\times \left[d\mathrm{e}^{-\lambda(2d+h-z)} - \int_0^d \mathrm{e}^{-\lambda(2d'+h-z)}\mathrm{d}d' \right]\mathrm{d}\lambda, \qquad (41)$$

where once again, the sinh function has been expanded in terms of exponents. The λ integration can be evaluated using Eq. (A3) from Appendix A, giving

$$M_\rho^2 = \frac{m_{TX}}{4\pi} \frac{(\mu\sigma)^2}{2} \left[\frac{d}{\rho}\left(-H_d + \sqrt{\rho^2 + H_d^2} \right) \right.$$
$$\left. - \frac{1}{\rho}\int_0^d \left(-H_d + \sqrt{\rho^2 + H_{d'}^2} \right)\mathrm{d}d' \right], \qquad (42)$$

where now $H_{d'} = 2d' + h - z$. Using Abramowitz and Stegun (1965), Eqs. (3.3.41) and (4.6.20), the d' integral can be evaluated, the final result being

$$M_\rho^2 = \frac{m_{TX}}{4\pi} \frac{(\mu\sigma)^2}{2} \frac{1}{4\rho} \left[4d\sqrt{\rho^2 + H_d^2} - 4d^2 \right.$$
$$- H_d\sqrt{\rho^2 + H_d^2} + H_h\sqrt{\rho^2 + H_h^2}$$
$$\left. - \rho^2\mathrm{asinh}\left(\frac{H_d}{\rho}\right) + \rho^2\mathrm{asinh}\left(\frac{H_h}{\rho}\right) \right]. \qquad (43)$$

These two analytic solutions, Eqs. (40) and (43), have been compared with numerical integration of Eq. (32) and the results agree to computational accuracy (Fig.
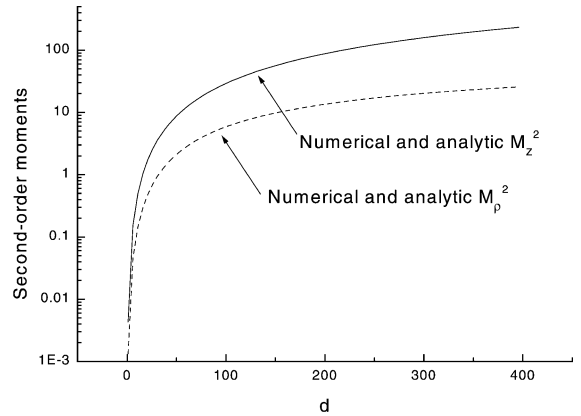

Fig. 3. The second-order moments for the same geometric configuration as shown in Fig. 2, setting $\frac{m}{4\pi}\frac{(\mu\sigma)^2}{2} = 1$. The analytic expressions (Eqs. (40) and (43)) plot on top of the results derived by numerical integration of Eq. (32).

3). The integrals for the higher-order moments of the thick layer do not exist.

2.1. Limiting case 1: the thin sheet

In the limit, as the thickness becomes thin, $d \rightarrow 0$ but the conductivity–thickness product remains finite. Hence, ud is small and we can set $\tanh(ud) \rightarrow ud$, and $1 + d\lambda \rightarrow 1$ (Wait, 1982). Hence, we can simplify the expression for $f(z)$ in Eq. (14), to get

$$f(z) = \frac{z}{\frac{2\lambda}{\mu\sigma d} - z}. \qquad (44)$$

From which, it is straightforward to show that

$$I_r^1 = f^1(0) = \frac{\mu\sigma d}{2\lambda}, \qquad (45)$$

$$I_r^2 = f^2(0) = \frac{(\mu\sigma d)^2}{2\lambda^2}, \qquad (46)$$

$$I_r^3 = f^3(0) = \frac{3(\mu\sigma d)^3}{4\lambda^3}. \qquad (47)$$

The first-order moment integrals can be written in the form

$$M_j^1 = \frac{m_{TX}}{4\pi} \frac{\mu\sigma d}{2} \frac{\partial}{\partial z}\int_0^\infty \mathrm{e}^{-\lambda(h-z)}J_l(\lambda\rho)\mathrm{d}\lambda. \qquad (48)$$

Once again, the λ integration can be evaluated using Eqs. (A1) and (A2), which can subsequently be differentiated to give

$$M_z^1 = \frac{m_{TX}}{4\pi} \frac{\mu\sigma d}{2} \frac{z-h}{(\rho^2 + (z-h)^2)^{3/2}}. \qquad (49)$$

$$M_\rho^1 = \frac{m_{TX}}{4\pi} \frac{\mu\sigma d}{2} \frac{\rho}{(\rho^2 + (z-h)^2)^{3/2}}. \qquad (50)$$

The second-order moments are of the form

$$M_j^2 = \frac{m_{TX}}{4\pi} \frac{(\mu\sigma d)^2}{2} \int_0^\infty e^{-\lambda(h-z)} J_l(\lambda\rho) \mathrm{d}\lambda, \qquad (51)$$

which can be evaluated using Eqs. (A1) and (A2), to give

$$M_z^2 = \frac{m_{TX}}{4\pi} \frac{(\mu\sigma d)^2}{2} \frac{1}{\sqrt{\rho^2 + (z-h)^2}}, \qquad (52)$$

$$M_p^2 = \frac{m_{TX}}{4\pi} \frac{(\mu\sigma d)^2}{2} \frac{1}{\rho} \left[1 - \frac{h-z}{\sqrt{\rho^2 + (z-h)^2}} \right]. \qquad (53)$$

The third-order moments are of the form

$$M_j^3 = \frac{m_{TX}}{4\pi} \frac{3(\mu\sigma d)^3}{4} \int_0^\infty \frac{1}{\lambda} e^{-\lambda(h-z)} J_l(\lambda\rho) \mathrm{d}\lambda. \qquad (54)$$

The third-order moment for the z component does not exist, but the ρ moment can be evaluated using Eq. (A3) to give

$$M_\rho^3 = \frac{m_{TX}}{4\pi} \frac{3(\mu\sigma d)^3}{4} \frac{1}{\rho}$$
$$\times \left[\sqrt{\rho^2 + (h-z)^2} - (h-z) \right]. \qquad (55)$$

These thin-sheet expressions have all been verified by comparing the results from a numerical evaluation of the moment integral with the retreating image solution used to generate the impulse response.

2.2. Limiting case 2: the half space

In the limit of $d \to \infty$, it can be seen from Eq. (19) that

$$I_r^1 \to \frac{\mu\sigma}{4\lambda^2}, \qquad (56)$$

so that

$$M_j^1 = \frac{m_{TX}}{4\pi} \frac{\mu\sigma}{4} \int_0^\infty e^{-\lambda(h-z)} J_l(\lambda\rho) \mathrm{d}\lambda, \qquad (57)$$

and hence, using Eqs. (A2) and (A1), we have

$$M_\rho^1 = \frac{m_{TX}}{4\pi} \frac{\mu\sigma}{4} \frac{1}{\rho} \left[1 - \frac{h-z}{\sqrt{\rho^2 + (h-z)^2}} \right], \qquad (58)$$

$$M_z^1 = \frac{m_{TX}}{4\pi} \frac{\mu\sigma}{4} \frac{1}{\sqrt{\rho^2 + (h-z)^2}}. \qquad (59)$$

The formula for M_ρ^1 agrees with the resistive-limit formula derived by Annan et al. (1996) and the formula for M_z^1 can also be obtained by setting $d = \infty$ in Eq. (31). For the half space, the integrals for higher-order moments do not exist.

3. Conductance estimation

The moments for a thin sheet (Eqs. (49), (50), (52), (53) and (55)) are all in the form

$$M_j^n = c_n (\mu\sigma d)^n T_j^n(\rho, h, z), \qquad (60)$$

where c_n is a constant, and T_j^n is a geometric function with a simple analytic form. The geometric function is dependent only on h, ρ and z. The receiver height, z, is also dependent on the height, $z = -(h - v)$, where v is the vertical offset of the transmitter from the receiver. All these parameters are known, so the conductance σd can be calculated simply from

$$\sigma d = \frac{1}{\mu} \sqrt[n]{\frac{M_j^n}{c_n T_j^n}}. \qquad (61)$$

The moments of the impulse response have been calculated from MEGATEM™ data collected over the OTH test site (Ontario Geological Survey, 2000), also presented in Smith and Lee (in press). Estimates of the conductance have been obtained for the first-, second- and third-order moments of the ρ component. These estimates have been plotted as grey scale images in Fig. 4. The left image is the conductance derived from the first-order moment. This image will be similar to
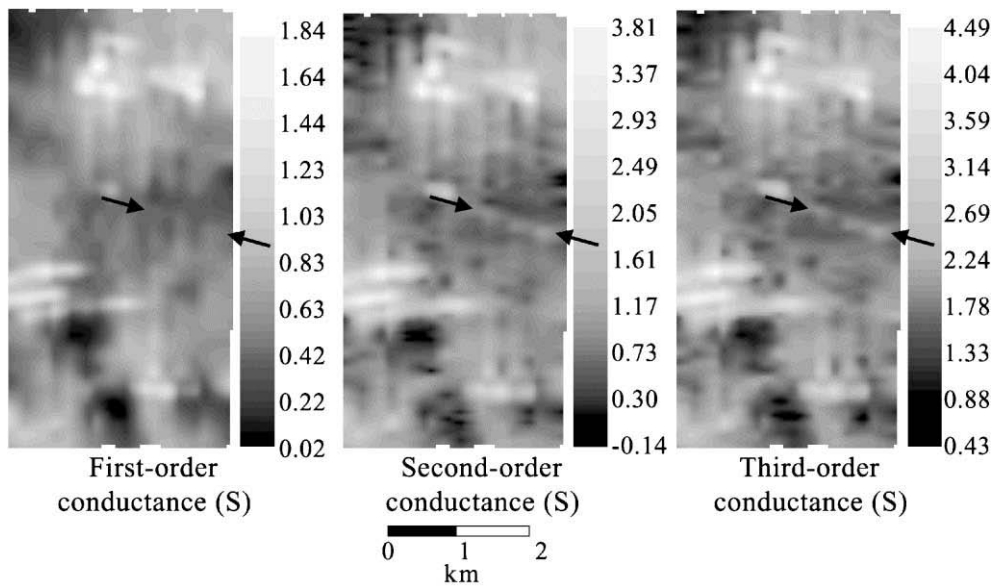
Fig. 4. The conductance images derived from the first- second- and third-order moments (left, centre and right, respectively) for a MEGATEM survey over the Read-Mahaffy test site. A linear conductor buried about 100 m below the glacial cover lies between the arrows on each image. Note that the data range is different for each image but even so, the deep conductor is more apparent on the higher-order images. The image is stretched using Gaussian equalization. For colour versions of these images see the 'Electronic Supplements' at the journal's homepage, http://www.elsevier.com/locate/jappgeo.

what would be derived using the method of Smith (2000), except that the effect of a finite off time has not been taken into account. The middle image of Fig. 4 is from the second-order moment and the right image is from the third-order moment. Each image is very similar, except the data range varies somewhat from image to image and each estimation method has varying success in identifying a conductor at about 100-m depth. This conductor lies between the black arrows shown on each image. The conductor is barely apparent on the first-order conductance—the indicated zone appears like a contact with conductive material to the south and more resistive material to the north. On the second-order image, there is a better indication of a discrete feature; and on the third-order image, the deep conductor is slightly more apparent. This indicates that higher-order moments may be better at identifying deep conductors. The sensitivity of each moment to material at different depths can be better understood by calculating how sensitive the moment is to adding a 5-m layer of material at a depth d. The incremental change in the moment ΔM, resulting from adding this thin layer has been plotted in Fig. 5, where

the incremental change has been normalized by the moment M. The incremental changes in the first moment are large at shallow depth, but drop below
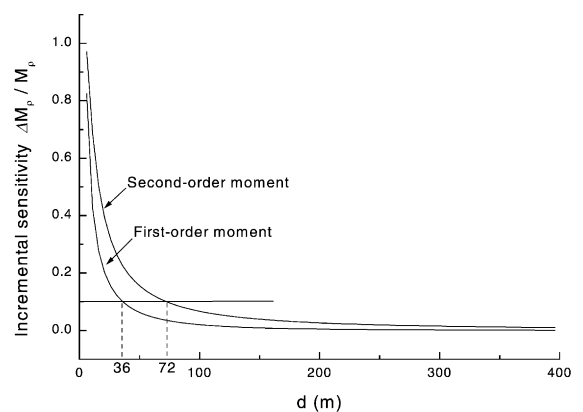

Fig. 5. The normalized incremental change in the moment as a consequence of adding a 5-m thick layer to a layer of thickness d. The incremental change in the normalized moment becomes small (less than 0.1), when the layer thickness is greater than 36 or 72 m for the first and second moments, respectively.
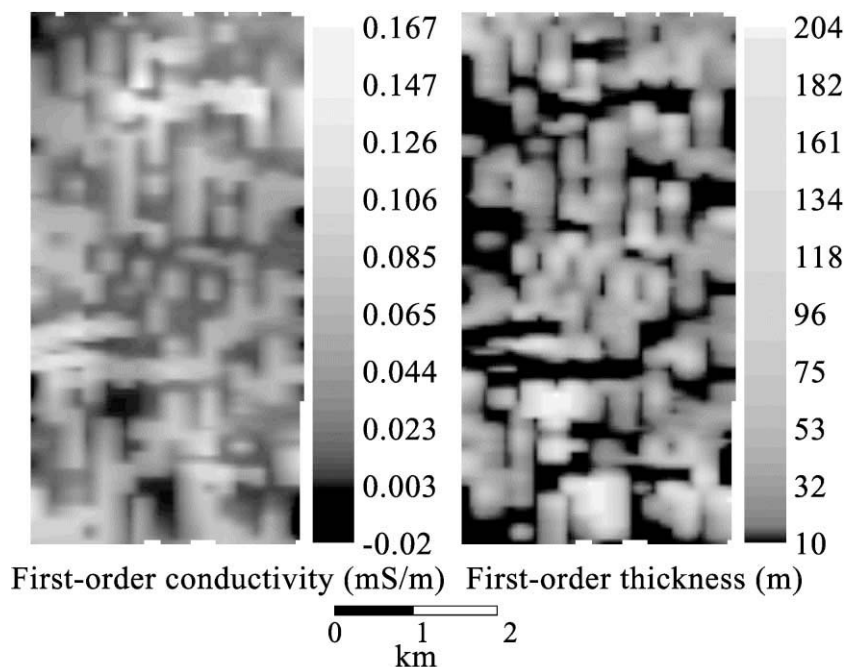
Fig. 6. The conductivity (left) and thickness (right) derived from the first-order ρ and z component moments, for the same survey area as shown in Fig. 4. The presentation highlights lateral changes associated with east–west striking features. For colour versions of these images see the 'Electronic Supplements' at the journal's homepage, http://www.elsevier.com/locate/jappgeo.

0.1 at depths greater than 36 m. The second moment is more sensitive to deeper material, as the incremental change does not drop below 0.1 until the depths are greater than 72 m. Note that these depth sensitivity curves have a shape that is independent of the conductivity.

Images for the conductance can also be derived from the first- and second-order z component moments. These will look similar, except in the vicinity of vertical conductors, the vertical component response is a negative trough flanked by two positive peaks (Smith and Lee, 2001).

4. Conductivity estimation

The half space moments (Eqs. (58) and (59)) are in the form

$$M_j^1 = b_1(\mu\sigma)\eta_j(\rho, h, z), \tag{62}$$

where b_1 is a constant and η_j is a half space geometric function, again with a simple analytic form. As before the conductivity, σ can be calculated simply from

$$\sigma = \frac{1}{\mu} \frac{M_j^1}{b_1 \eta_j}. \tag{63}$$

These estimates should look similar to the thin-sheet conductances also estimated from the first-order moment (e.g. the left image of Fig. 4).

5. Conductivity depth estimation

For the conductance and conductivity cases discussed above, each equation involved only one unknown, so solving for that unknown is straight forward. The equations for the thick layer moments involve two unknowns, the conductivity and thickness. If two or more of the measured moments are used as known quantities, then it should be possible to estimate the conductivity and thickness. One strategy

would be to use the equations for the first- and second-order moments for one component; however, our previous observation is that different moments are sensitive to a different depth (i.e. thickness) so the estimation process will become problematic. Another strategy is to use the ρ and z components for one moment. As an example, we have varied the thickness d between 10 and 200 m and then derived two estimates of the conductivity, one from M_ρ^1 and one from M_z^1. The depth at which the two estimates are closest is used as the estimate for the depth, and the estimate for the conductivity is the average of the conductivities derived from M_ρ^1 and M_z^1 and at this depth. These two quantities are imaged in Fig. 6. Compared with the first-order conductance image, the conductivity and the thickness images show strong east–west striking features. These are believed to result from the two components often having response profiles with different shapes over a discrete conductive feature. This means that the layered model is inappropriate to explain the relative magnitudes of M_ρ^1 and M_z^1, so the thickness becomes either very large or very small, with corresponding changes in the conductivity. Although the overburden thickness and conductivity might not have been imaged well, the lateral heterogeneities, such as the deep conductor discussed previously, are apparent. In some survey areas, where the lateral changes in conductivity and/or thickness are gentler, the conductivity and thickness estimates might be much better. However, from this example, we conclude that this imaging strategy appears to give unstable results. An alternate strategy involving higher-order moments is required. In order to calculate these higher-order moments, it is necessary to take into account the finite off time and repetitive nature of the waveform.

6. Conclusions

Analytic solutions for the moments of the impulse response for a thick layer model have been obtained for moments of orders 1 and 2. In the limiting cases of a thin sheet, analytic solutions have been derived for the longitudinal component (moments 1, 2 and 3) and the vertical component (moments 1 and 2). In the limiting case of a half space, analytic solutions exist for the first-order moment only (both components).

Table 1
Summary of equation numbers where the final expression for each moment can be found (blank spaces imply there is no analytic expression)

	Thick slab	Thin sheet	Half space
M_ρ^0	Eq. (25)	Eq. (25)	Eq. (25)
M_z^0	Eq. (27)	Eq. (27)	Eq. (27)
M_ρ^1	Eq. (30)	Eq. (50)	Eq. (58)
M_z^1	Eq. (31)	Eq. (49)	Eq. (59)
M_ρ^2	Eq. (43)	Eq. (53)	
M_z^2	Eq. (40)	Eq. (52)	
M_ρ^3		Eq. (55)	

The equation number of the final expression for each of these moments is summarized in Table 1.

For the thin sheet and half space models, the moment equations can be inverted analytically and used to estimate a conductance or a conductivity. The images derived in this way have all been presented without any cosmetic filtering, indicating that estimating conductances and conductivities from the moments is a stable process.

Two moment equations can be used to estimate the conductivity and the depth. In the example presented, the resulting images were quite good at highlighting lateral changes in the conductivity structure.

Incremental increases in the thickness of the layer show that material at greater depths has more influence on the second-order moment than the first moment. This is consistent with the images of the conductivity derived from the higher-order moments showing a deeper conductor more clearly.

Appendix A

The Lipschitz related integrals are (Wait, 1982, pp. 117 and 118)

$$\int_0^\infty e^{-\lambda a} J_0(\lambda\rho)d\lambda = \frac{1}{\sqrt{\rho^2 + a^2}}, \qquad (A1)$$

$$\int_0^\infty e^{-\lambda a} J_1(\lambda\rho) d\lambda = \frac{1}{\rho}\left[1 - \frac{a}{\sqrt{\rho^2 + a^2}}\right], \qquad (A2)$$

and

$$\int_0^\infty \frac{e^{-\lambda a}}{\lambda} J_1(\lambda\rho) d\lambda = \frac{1}{\rho}\left[\sqrt{\rho^2 + a^2} - a\right]. \qquad (A3)$$

References

Abramowitz, M., Stegun, I.A., 1965. Handbook of Mathematical Functions. Dover, New York, 1046 pp.

Anderson, W.L., 1979. Numerical integration of related Hankel transforms of order 0 and 1 by adaptive digital filtering. Geophysics 44, 1287–1305.

Annan, A.P., Smith, R.S., Lemieux, J., Pedersen, R.N., 1996. Resistive-limit, time-domain AEM apparent conductivity. Geophysics 61, 93–99.

Carslaw, H.S., Jaeger, J.C., 1959. Conduction of Heat in Solids Oxford, 510 pp.

Christensen, N.B., 1990. Optimized fast Hankel transform filters. Geophysical Prospecting 38, 545–568.

Grant, F.S., West, G.F., 1965. Interpretation Theory in Applied Geophysics. McGraw-Hill, New York, 584 pp.

Johansen, H.K., Sorensen, K., 1979. Fast Hankel transforms. Geophysical Prospecting 27, 876–901.

Macnae, J., King, A., Stolz, N., Osmakoff, A., Blaha, A., 1998. Fast AEM data processing and inversion. Exploration Geophysics 29, 163–169.

Macnae, J., King, A., Stolz, N., Klinkert, P., 1999. 3-D EM inversion to the limit. In: Oristaglio, M., Spies, B. (Eds.), Three-dimensional electromagnetics. Society of Exploration Geophysicists, Tulsa, Geophysical Development Series, vol. 7, pp. 489–501.

Mohsen, A.A., Hashish, E.A., 1994. The fast Hankel transform. Geophysical Prospecting 42, 131–139.

Ontario Geological Survey, 2000. Airborne magnetic and electromagnetic surveys, Reid-Mahaffy airborne geophysical test site survey. Sudbury, Ontario Geological Survey, Miscellaneous Release–Data (MRD)-55, 50 pp.

Smith, R.S., 2000. The realizable resistive limit: a new concept for mapping geological features spanning a broad range of conductances. Geophysics 65, 1124–1127.

Smith, R.S., Lee, T.J., 2002. The moments of the impulse response: a new paradigm for the interpretation of transient electromagnetic data. Geophysics, in press.

Smith, R.S., Lee, T.J., 2001. The impulse-response moments of a conductive sphere in a uniform field, a versatile and efficient electromagnetic model. Exploration Geophysics 32, 113–118.

Wait, J.R., 1982. Geoelectromagnetism. Academic Press, New York, 268 pp.

Ward, S.H., Hohmann, G.W., 1988. Electromagnetic theory for geophysical applications. In: Nabighian, M.N. (Ed.), Electromagnetic Methods in Applied Geophysics—Theory. Volume I, Investigations in Geophysics, vol. 3. Society of Exploration Geophysicists, Tulsa, pp. 130–311.